Immunity, Volume *47*

Supplemental Information

Defined Sensing Mechanisms and Signaling Pathways Contribute to the Global Inflammatory Gene Expression Output Elicited by Ionizing Radiation

Prabhat K. Purbey, Philip O. Scumpia, Peter J. Kim, Ann-Jay Tong, Keisuke S. Iwamoto, William H. McBride, and Stephen T. Smale

Figure S1, Purbey et al.

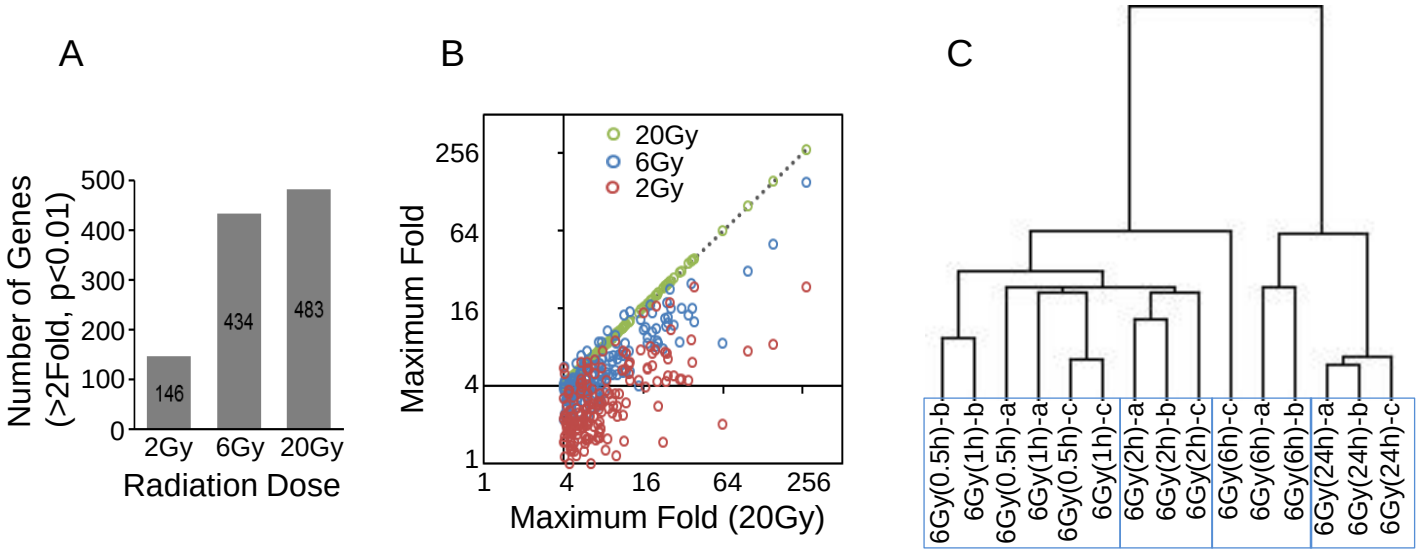

Figure S1 (Related to Figure 1). Dose Response Analysis of RNA-Seq Data From IR-Induced BMDMs.

As a first step toward a global analysis of the transcriptional cascade induced by IR, we performed RNA-seq with mRNA from mouse C57BL/6 BMDMs treated with 2, 6 and 20 Gy of IR for 0, 0.5, 1, 2, 6, and 24 hr (see STAR Methods).

(A) On average 146, 434 and 483 genes were induced more than 2-fold at peak expression by 2, 6, and 20 Gy IR ($p<0.01$; RPKM >3 in at least one time point; 3 replicates for all samples, except only 2 replicates for 2 Gy 24-hr time point).

(B) A dose response analysis is shown for the 176 genes induced >4-fold by 20 Gy IR. The average maximum fold-induction for each gene following 2 (red), 6 (blue), and 20 (green) Gy IR is plotted on the y-axis, in comparison to the maximum fold-induction by 20 Gy on the x-axis.

(C) Hierarchical clustering of RNA-seq data from the 3 individual biological replicates using 6 Gy IR shows the reproducibility of the results. Genes that were significantly induced by 6 Gy IR (average fold>2, $p<0.01$, RPKM>3, n=434) were examined in this analysis using the “Gene Clustering 3.0” program. The data sets from cells irradiated for 0.5 and 1 hr clustered together, indicating the close similarity between gene induction profiles at these early time points. The data sets from cells irradiated for 2, 6, and 24 hrs clustered separately and consistently.

Figure S2, Purbey et al.

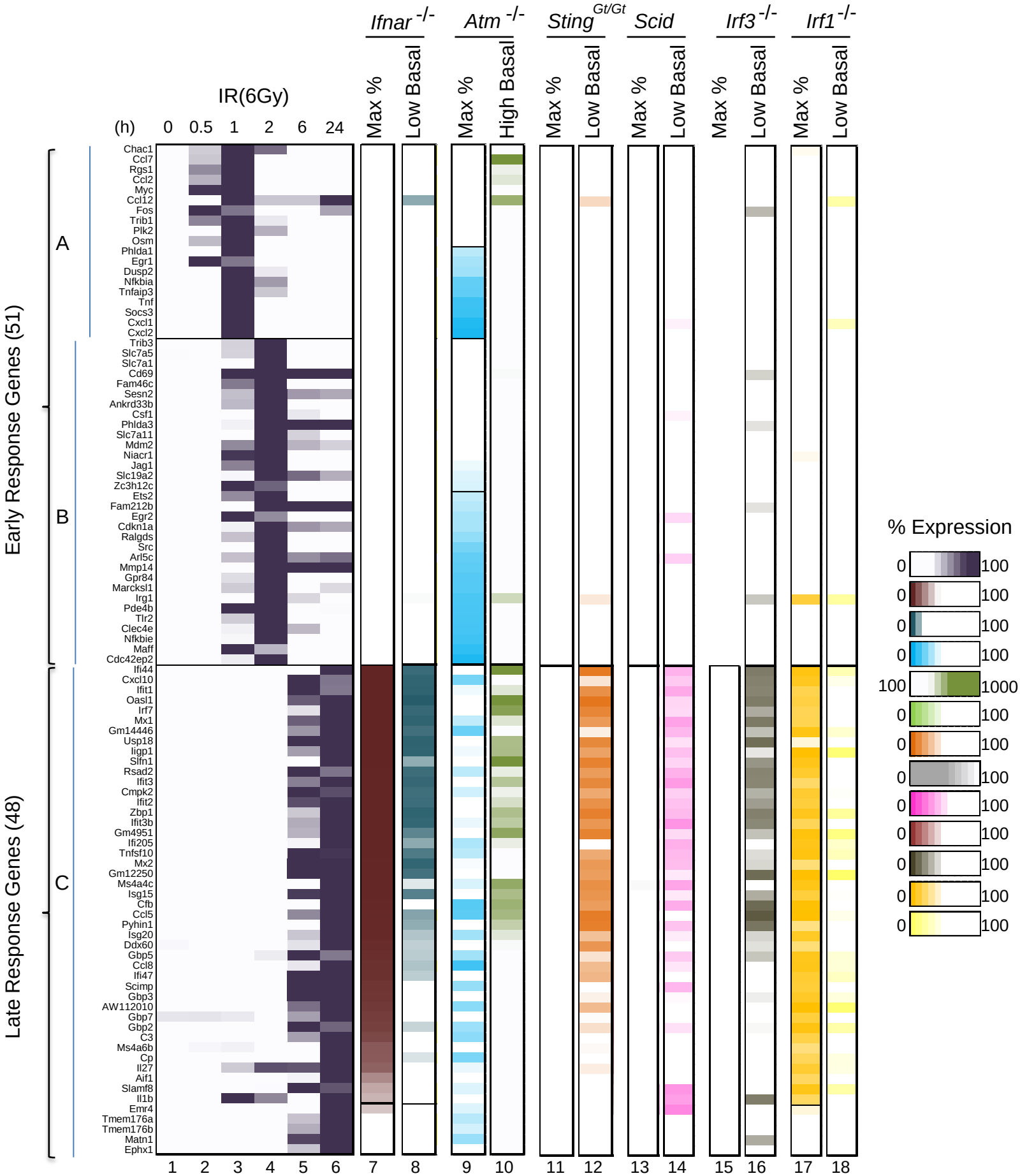

Figure S2 (Related to Figure 2). Summary of Maximum and Basal Transcript Levels for the 99 IR-Induced Genes in WT BMDMs and BMDMs from 6 Mutant Mouse Strains.

The heat maps shown here reproduce the results shown in Figures 2A, 3A, and 4C, but with specific names of the 99 genes shown.

Figure S3, Purbey et al.

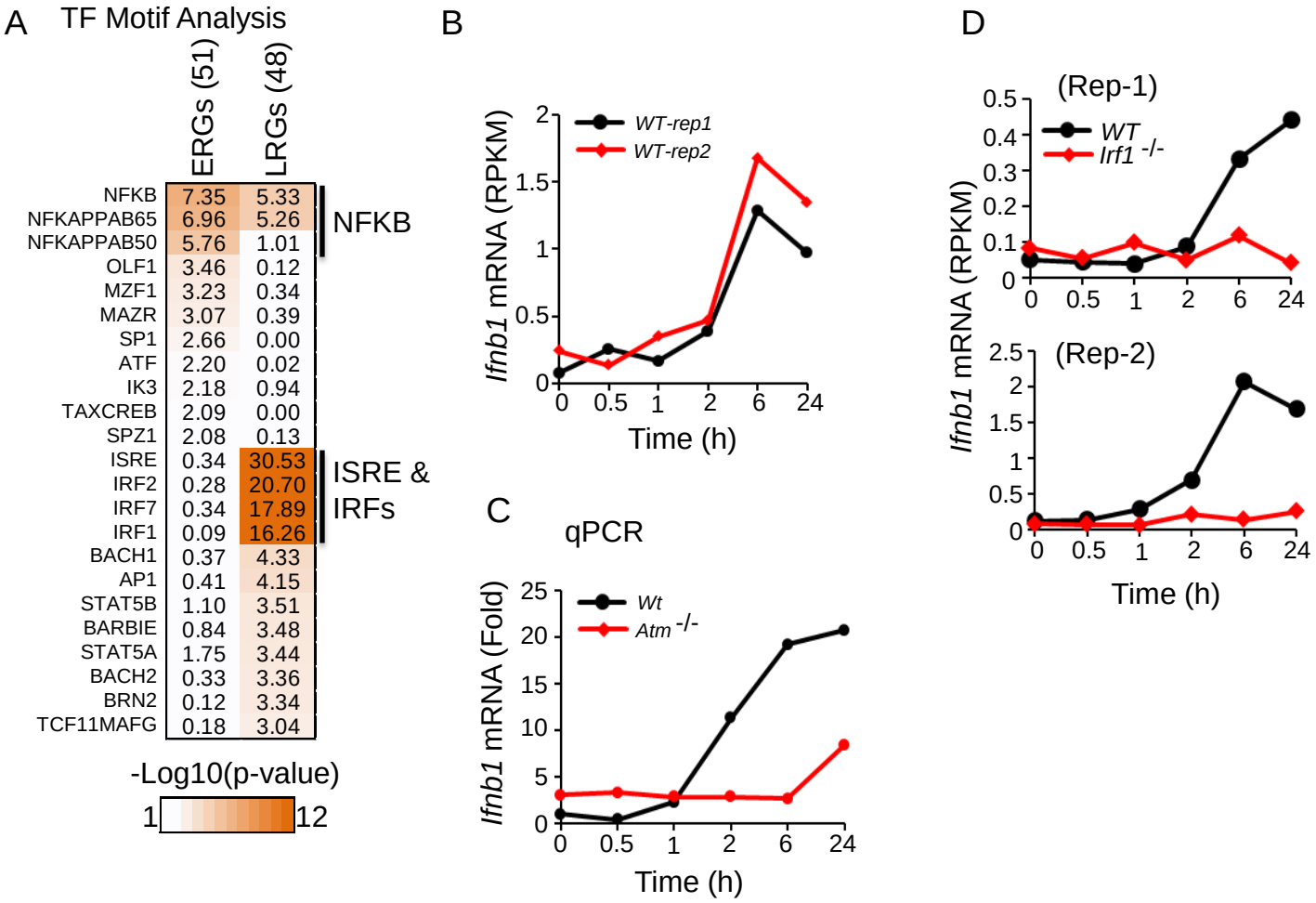

Figure S3 (Related to Figure 2). Transcription Factor Motif Analysis for IR-Induced ERGs and LRGs, and *Ifnb1* Expression Kinetics in WT and Mutant BMDMs.

(A) Analysis of over-represented transcription factor binding motifs in the promoters of ERGs and LRGs. The heat map shows the "-Log10(p-value)" for the over-represented transcription factors. The color scale used is shown at the bottom.

(B) The line graph shows the *Ifnb1* mRNA kinetics (in RPKM) from two RNA-seq replicates.

(C) The line graph shows the *Ifnb1* mRNA kinetics in WT (black) and *Atm*$^{-/-}$ (red) BMDMs. Relative mRNA levels were measured by qRT-PCR, with average values from 2 biological replicates shown.

(D) The line graph shows the *Ifnb1* mRNA kinetics (in RPKM) from 2 biological RNA-seq replicates comparing WT and *Irf1*$^{-/-}$ BMDMs.

Figure S4, Purbey et al.

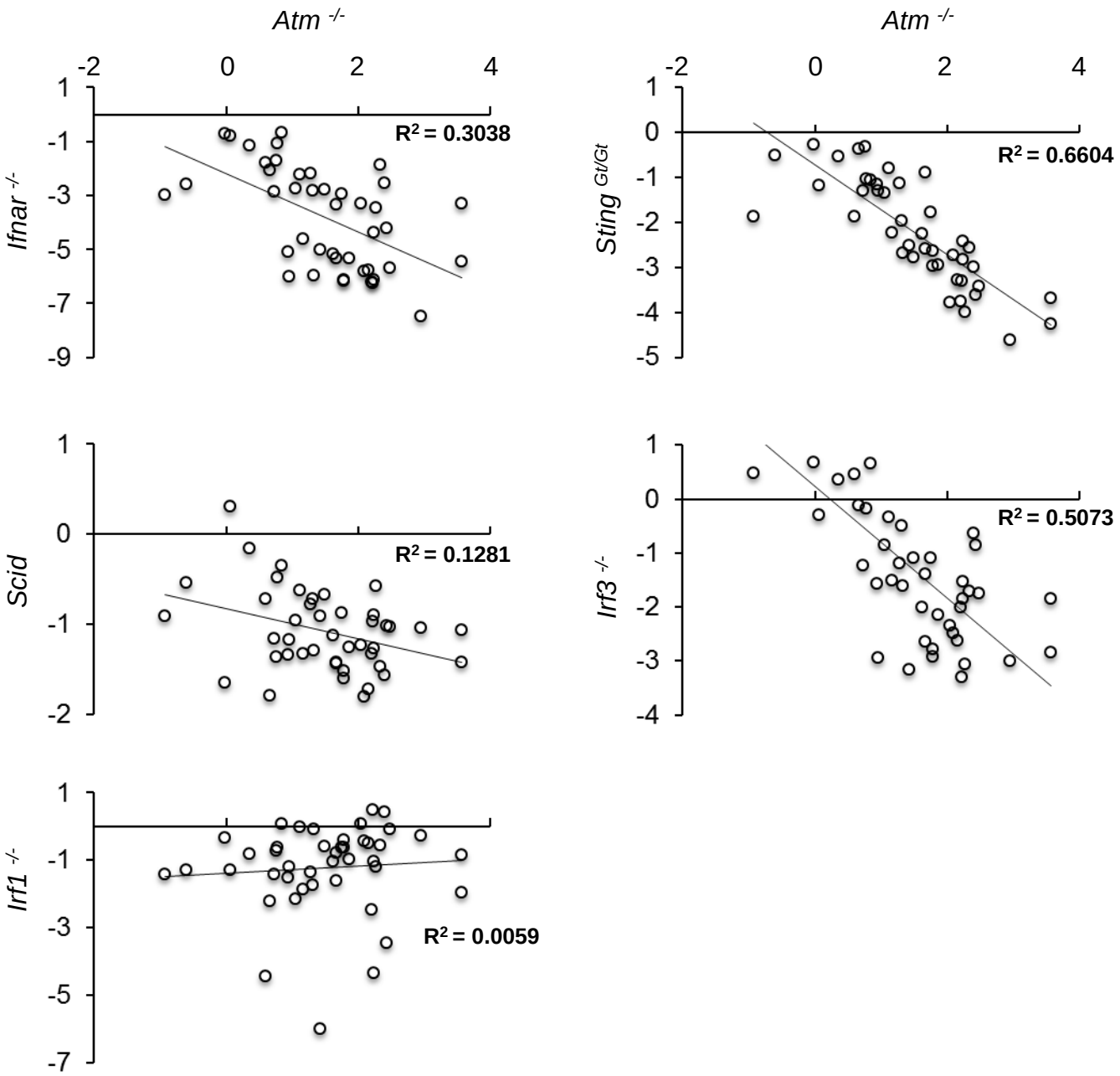

Figure S4 (Related to Figure 3). Statistical Comparison between High Basal Transcript Levels in *Atm*$^{-/-}$ BMDMs and Low Basal Transcript Levels in *Ifnar*$^{-/-}$, *Sting*$^{Gt/Gt}$, *Scid*, *Irf3*$^{-/-}$, and *Irf1*$^{-/-}$ BMDMs.

Shown are scatter plots between high basal transcript levels (log2 fold change) in *Atm*$^{-/-}$ BMDMs on the x-axis and low basal transcript levels (log2 fold change) in *Ifnar*$^{-/-}$, *Sting*$^{Gt/Gt}$, *Scid*, *Irf3*$^{-/-}$, and *Irf1*$^{-/-}$ BMDMs on the y-axis. Linear regression analysis was used to determine the correlation coefficient (R2) for each pair. A high percentage of data points supported the negative relationship between *Atm*$^{-/-}$ and *Sting*$^{Gt/Gt}$ (66.0%), *Irf3*$^{-/-}$ (50.7%), and *Ifnar*$^{-/-}$ (30.4%). A modest percentage of data points also supported the negative relationship between *Atm*$^{-/-}$ and *Scid* (12.8%). In contrast, a poor relationship was observed with *Irf1*$^{-/-}$ (0.59%).

Figure S5, Purbey et al.

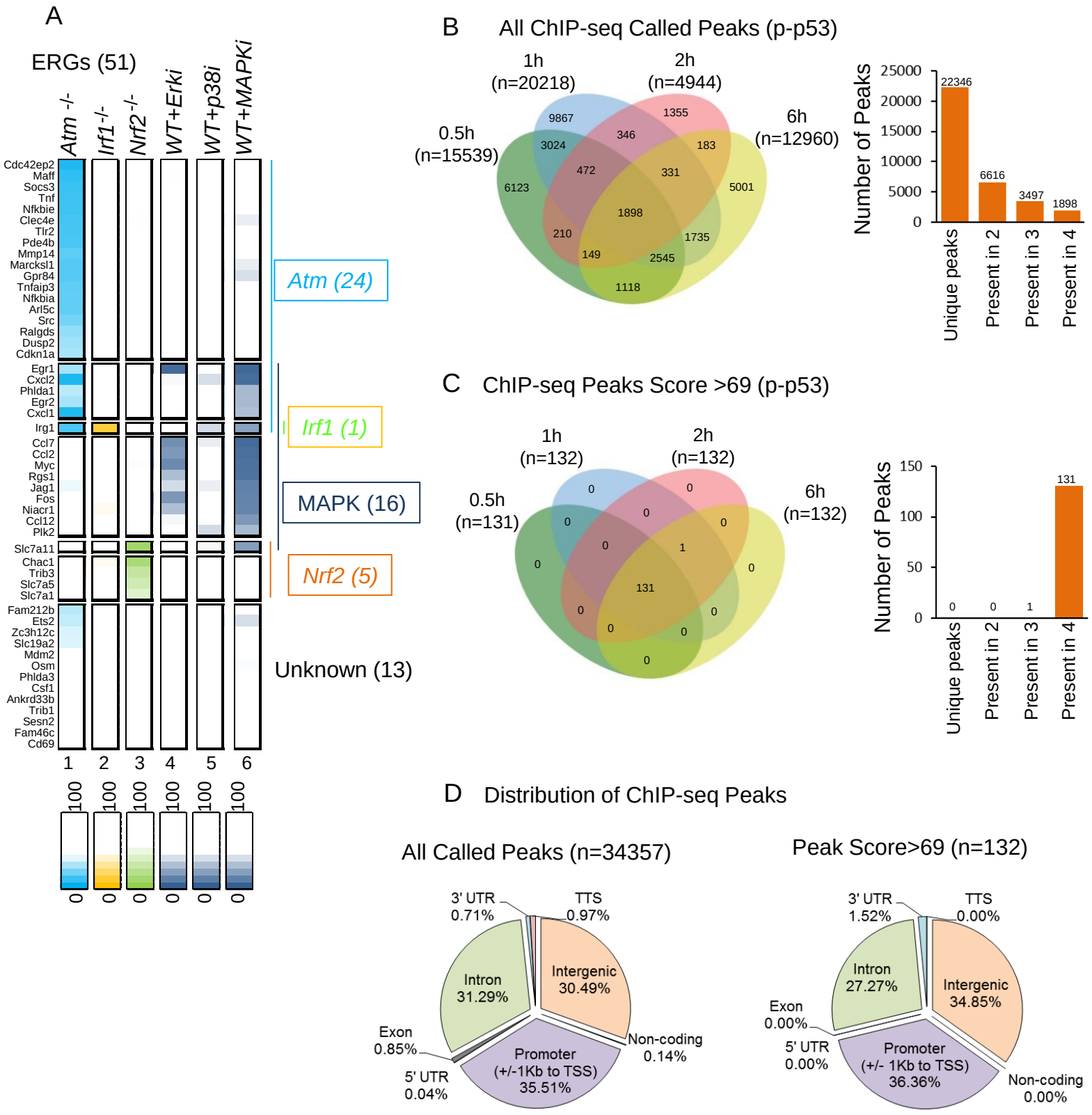

Figure S5 (Related to Figure 5). Basic Analysis of p-p53 ChIP-Seq Data Sets.

(A) The heat map shows the impact of individual inhibitors of the ERK (column 4) and p38 (column 5) MAPKs on IR-induced expression of ERGs in comparison to the impact of the 2 inhibitors when combined (column 6).

(B) A Venn diagram represents the total number of called peaks (HOMER, Heinz et al., 2010) and their overlap from the phospho-p53 ChIP-seq experiments at 0.5, 1, 2, and 6 hr post-irradiation. The histogram at the right displays the number peaks uniquely present in one sample (22346), overlapping in at least two (6616), overlapping in three (3497) and overlapping all four (1898) samples.

(C) A Venn diagram shows the distribution and overlap of strong p-p53 binding peaks (peak score >69, n=132). All of these strong peaks but one were present in all 4 samples, as shown in the right histogram.

(D) The left and right pie charts display the genomic distribution of all p-p53 ChIP-seq peaks (n=34357) and the strongest peaks (score >69; n=132) in Promoters (+/- 1kb from TSS), 5' UTRs, Exons, Introns, Transcription termination sites (TTSs), Intergenic regions, and Non-coding regions.

Figure S6, Purbey et al.

UCSC ChIP-seq (p-p53) and RNA-seq (*WT* and *p53-/-*) profile of p53 target genes.

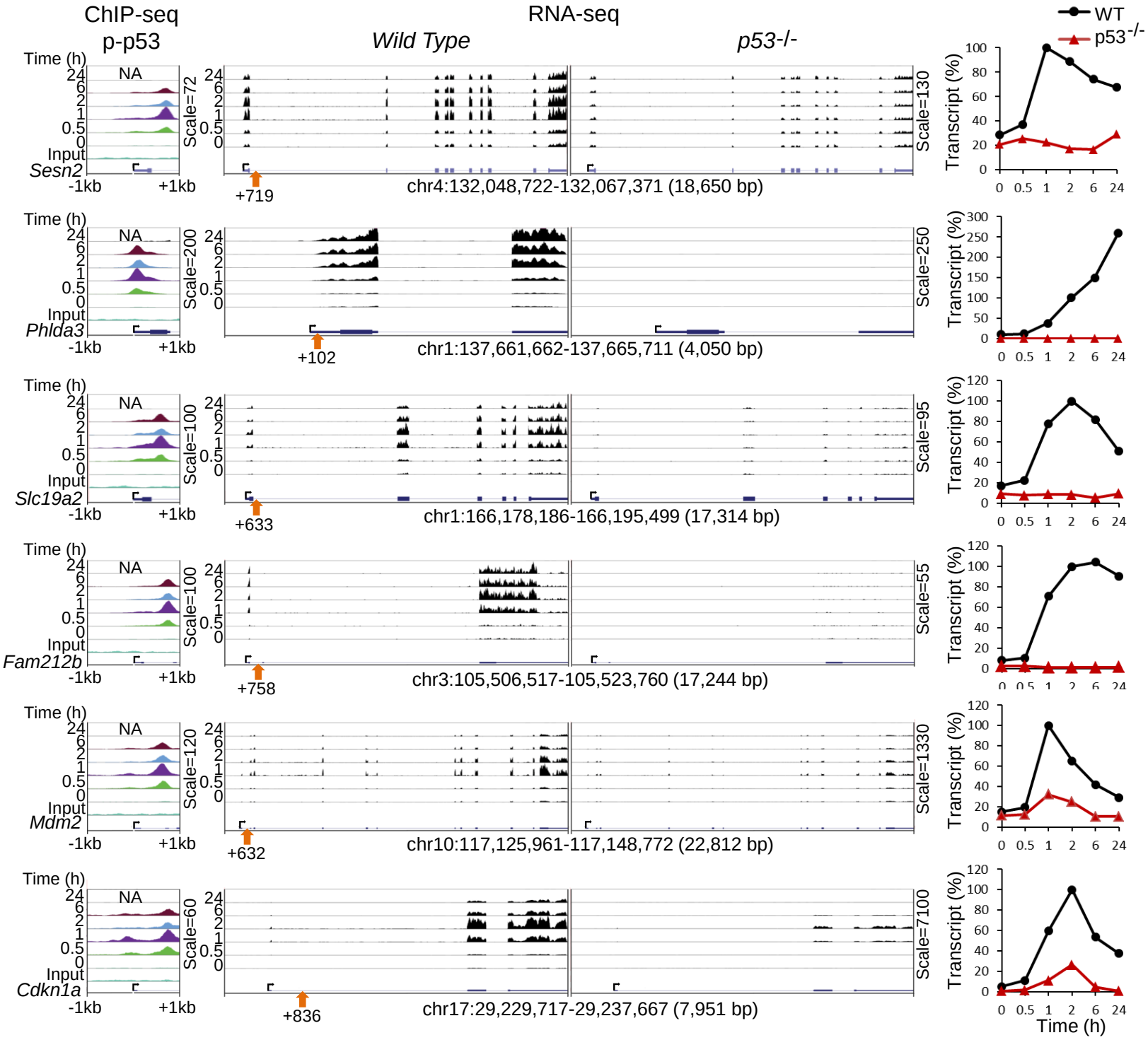

Figure S6 (Related to Figure 7). Detailed Analysis of the 6 ERGs Exhibiting Strong p53 Dependence: Consistent Binding of p-p53 Downstream of the TSSs.

The left panel displays genome browser normalized tracks for the binding of p-p53 within 1kb of the TSSs for the 6 p53-dependent ERGs in BMDMs treated with 6 Gy IR for 0, 0.5, 1, 2, and 6 hr. ChIP-seq was not performed at the 24-hr time point and therefore is indicated as Not Available (NA). The middle panel shows the genome browser tracks of RNA-seq data for the indicated time points (0, 0.5, 1, 2, 6, and 24 hr) in WT (middle left panel) and *p53*$^{-/-}$ (middle right panel) BMDMs. The genome browser windows for the RNA-seq tracks extend from -1kb relative to the TSS to the end of the genes. Orange arrows point to the p-p53 ChIP-Seq summits, which were located downstream of the TSS in all 6 genes. The extreme right panels represent normalized expression kinetics (maximum percent expression relative to WT) for each of the 6 genes in WT (black) and *p53*$^{-/-}$ (red) BMDMs.

Figure S7, Purbey et al.

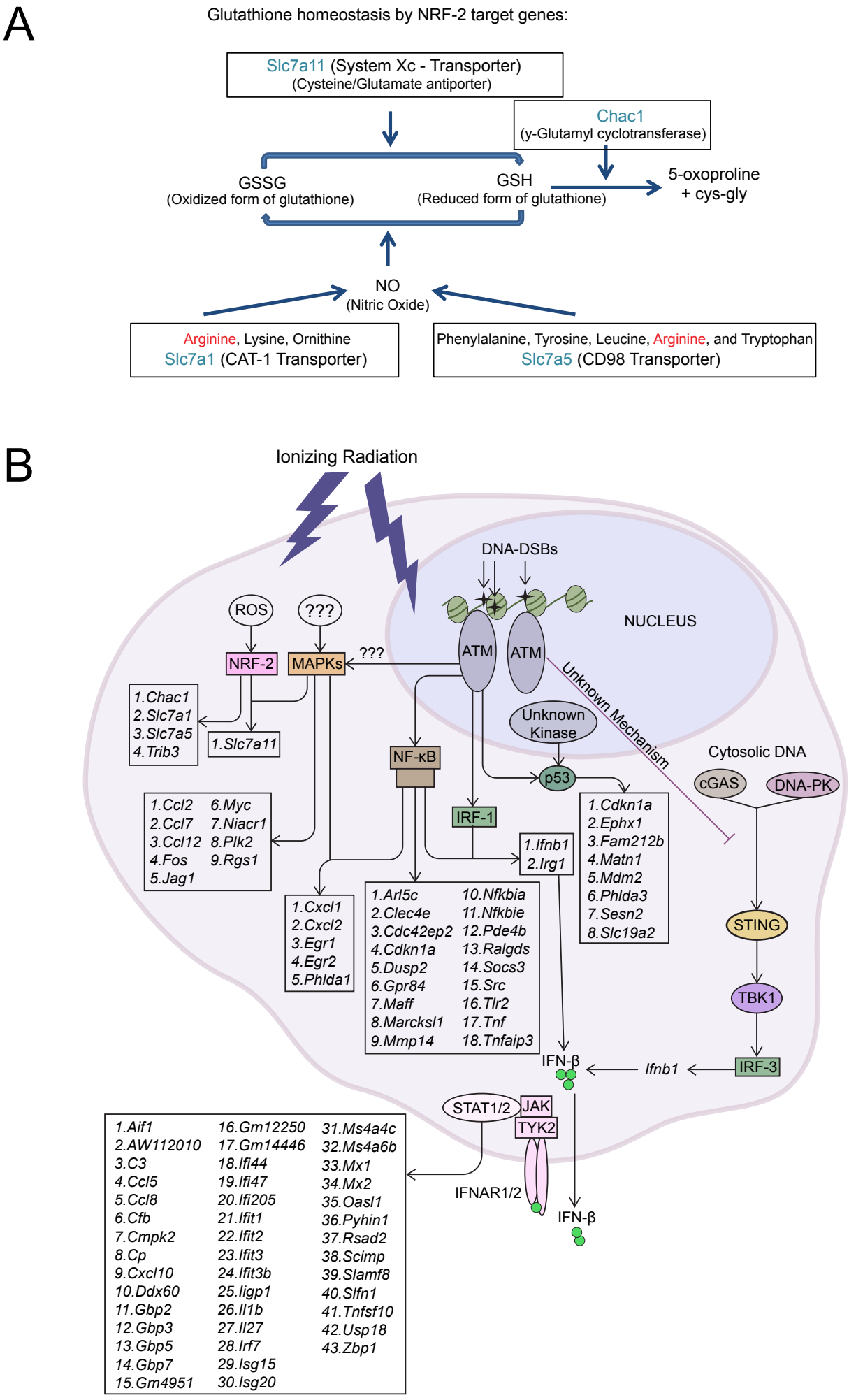

Figure S7 (Related to Figure 7). Final Model Figure and Schematic Representation of Glutathione Homeostasis Regulated by NRF-2 Target Genes.

(A) Slc7a11 forms System Xc- antiporter, which is important for the synthesis and maintenance of reduced glutathione (GSH). Slc7a1 forms CAT-1 transporter to transport arginine, lysine and ornithine. Slc7a5 forms the CD98 transporter, which transports phenylalanine, tyrosine, leucine, arginine and tryptophan. Arginine is a substrate for the synthesis of nitric oxide, which is a free radical involved in converting the reduced form of glutathione into the oxidized form (GSSG). Chac1 is a γ-glutamyl cyclotransferase, which catalyzes cleavage of reduced glutathione into 5-oxoproline and cys-gly dipeptide.

(B) A schematic model is shown that includes the key IR sensors, signaling pathways, transcriptional regulators, and potently induced target genes evaluated in this study.